ADVANCED ENERGY MATERIALS
www.advenergymat.de

Overcoming Phase-Purity Challenges in Complex Metal Oxide Photoelectrodes: A Case Study of $CuBi_2O_4$

Ronen Gottesman, Igal Levine, Markus Schleuning, Rowshanak Irani, Daniel Abou-Ras, Thomas Dittrich, Dennis Friedrich, and Roel van de Krol**

The widespread application of solar-water-splitting for energy conversion depends on the progress of photoelectrodes that uphold stringent criteria from photoabsorber materials. After investigating almost all possible elemental and binary semiconductors, the search must be expanded to complex materials. Yet, high structural control of these materials will become more challenging with an increasing number of elements. Complex metal-oxides offer unique advantages as photoabsorbers. However, practical fabrication conditions when using glass-based transparent conductive-substrates with low thermal-stability impedes the use of common synthesis routes of high-quality metal-oxide thin-film photoelectrodes. Nevertheless, rapid thermal processing (RTP) enables heating at higher temperatures than the thermal stabilities of the substrates, circumventing this bottleneck. Reported here is an approach to overcome phase-purity challenges in complex metal-oxides, showing the importance of attaining a single-phase multinary compound by exploring large growth parameter spaces, achieved by employing a combinatorial approach to study $CuBi_2O_4$, a prime candidate photoabsorber. Pure $CuBi_2O_4$ photoelectrodes are synthesized after studying the relationship between the crystal-structures, synthesis conditions, RTP, and properties over a range of thicknesses. Single-phase photoelectrodes exhibit higher fill-factors, photoconversion efficiencies, longer carrier lifetimes, and increased stability than nonpure photoelectrodes. These findings show the impact of combinatorial approaches alongside radiative heating techniques toward discovering highly efficient multinary photoabsorbers.

1. Introduction

Direct photoelectrochemical (PEC) water splitting has been widely investigated for almost half a century.[1–4] Its attractiveness lies in the fact that it is suitable for both centralized and decentralized production of "green" hydrogen. This versatile chemical fuel can be used on-site and on-demand but can also be stored and transported for off-site use.[5] However, practical PEC applications put stringent demands on photoabsorber materials in terms of efficiency, cost, and stability. Significant trade-offs have to be made, and this has thus far impeded the commercialization of PEC technology.[3,4] High solar to hydrogen conversion efficiencies approaching 20% have been achieved with photoelectrodes based on high-quality III–V semiconductors, such as $GaInP_2$ and GaAs.[6] However, their cost is likely to be prohibitive, and many of them suffer from instability under PEC operating conditions. The primary materials criteria are suitable bandgap energy to absorb a large fraction of solar photons with sufficient energies to enable water splitting, good electrical conductivity to enable photogenerated charge carrier extraction, favorable energy-band positions to enable carrier injection, and long-term stability in an aqueous environment.[4] Additionally, the material should be abundant and inexpensive in order to make PEC technology competitive with the chemical production of hydrogen from coal or natural gas. Almost all possible elemental and binary semiconductors have been investigated as photoelectrodes for water splitting, but none fulfill all the requirements. Therefore, the search will have to be expanded to ternary or even more complex materials.

Metal-oxides offer many unique advantages as photoabsorber materials for PEC water splitting.[7–9] They have a variety of

Dr. R. Gottesman, M. Schleuning, Dr. R. Irani, Dr. D. Friedrich, Prof. R. van de Krol
Institute for Solar Fuels
Helmholtz-Zentrum Berlin für Materialien und Energie GmbH
Hahn-Meitner-Platz 1, 14109 Berlin, Germany
E-mail: ronen.gottesman@helmholtz-berlin.de; roel.vandekrol@helmholtz-berlin.de

The ORCID identification number(s) for the author(s) of this article can be found under https://doi.org/10.1002/aenm.202003474.

DOI: 10.1002/aenm.202003474

Dr. I. Levine, Dr. T. Dittrich
Institute Silicon Photovoltaics
Helmholtz-Zentrum Berlin für Materialien und Energie GmbH
12489 Berlin, Germany

M. Schleuning, Prof. R. van de Krol
Institut für Chemie
Technische Universität Berlin
Straße des 17. Juni 124, 10623 Berlin, Germany

Dr. D. Abou-Ras
Department of Structure and Dynamics of Energy Materials
Helmholtz-Zentrum Berlin für Materialien und Energie GmbH
Hahn-Meitner-Platz 1, 14109 Berlin, Germany

band-gap energies in the visible spectrum, often show good photoelectrochemical stability in aqueous solutions, have low-toxicity, and can be comprised of many elements throughout the periodic table, many of which are abundant and inexpensive to produce.[7,8] However, their ionic nature leads to the formation of small polarons, causing carrier localization[10–12] and poor carrier transport properties compared to nonoxide semiconductors (e.g., Si, GaAs).[13,14] Consequently, metal oxide-based PEC devices have shown moderate efficiencies (<8%).[15,16] However, it is likely that multinary or complex metal oxide compositions with the desired properties will be found within the large space of possible compositions. Examples of this are found in the field of high-temperature metal oxide superconductors, which showed an increased transition temperature with an increasing number of elements.[17,18] This exciting prospect has generated extensive high-throughput and combinatorial efforts to accelerate the discovery and study of new complex metal oxides photoabsorbers for solar water splitting.[19–24]

However, with rapidly increasing efforts toward finding new ideal compositions of photoabsorbers with enhanced properties, the number of different cations is very probable to increase. The cations may vary widely in size, oxidation state, and vapor pressure under heating treatment conditions. Therefore, designing highly controlled synthesis routes toward highly crystalline, single-phase materials will become more challenging as the number of elements comprises the photoabsorber would increase.[25,26] Physical synthesis approaches (i.e., pulsed laser deposition, molecular beam epitaxy) of high-quality metal-oxides thin films have been developed and continuously improved in the past three decades.[27] Common denominators in these methods are the use of lattice-matched substrates materials, which enable epitaxial growth, and the ability to deposit and/or post-anneal at high temperatures (≤1000 °C). However, the majority of thin-film photoelectrodes are polycrystalline and involve the use of polycrystalline transparent conductive substrates with moderated thermal stabilities (≤550 °C) in their fabrication. Therefore, a gap between the desired reaction temperatures of metal oxides and practical fabrication conditions when using glass-based transparent conductive substrates with low thermal stability creates a bottleneck toward syntheses routes of high-quality (complex) metal-oxides thin film photoelectrodes.

It is imperative to overcome the bottleneck in relatively simple ways, to decrease defects and undesirable formation of secondary phases (i.e., impurities). While shallow defects may enhance the conductivity of the material, deeper gap states may lead to degraded properties, such as decreasing the carriers' lifetimes, limiting the photovoltage, and as a result reducing the PEC performance and stability. Furthermore, strain and stress in polycrystalline thin-films may lead to increased dislocation formation, which may further induce impurities segregation (many of which can be photoactive) at certain thicknesses.[28,29] Photoactive impurities that are uncontrollably formed and randomly intermixed with the desired photoabsorber material can be harmful to the device's performance, properties, and stability. Therefore, a fabrication approach is needed that enables the high-controlled synthesis of single-phase complex metal oxide thin films over a range of thicknesses,[30] allowing for uniform thermal processing without affecting the properties of the transparent conductive substrate. A sensible immediate approach to finding routes to overcome the numerous challenges in synthesizing complex metal oxides would be to concentrate our efforts on a known multinary photoabsorber, such as $CuBi_2O_4$, as a case study material.

The ternary p-type semiconductor $CuBi_2O_4$ was first identified through a high-throughput, combinatorial study as a possible photocathode material for PEC water splitting.[31] Pure $CuBi_2O_4$ has a bandgap of 1.9 ± 0.05 eV,[32] corresponding to a maximum theoretical photocurrent density of about 17 mA cm^{-2}, and its conduction band minimum (CBM) is positioned at a more negative potential than the thermodynamic potential for water reduction, enabling solar H_2 production,[32–34] and presumably reduction of CO_2 as well.[35,36] Furthermore, with a valence band minimum (VBM) at more positive potentials than that of other photocathode materials and an unusually positive photocurrent onset potential of ≈1–1.2 V versus RHE,[32,33] it offers the possibility generate a photovoltage greater than 1 V for H_2 evolution, without the use of buffer layers or buried junctions.[37] Therefore, its attractive electronic properties mark $CuBi_2O_4$ as a prime candidate for efficient solar water splitting.[38]

The phase diagram of Bi_2O_3 and CuO (Figure S1, Supporting Information) displays two major challenges in the fabrication of $CuBi_2O_4$ thin films photoelectrodes.[39–41] First, the solid-state reaction of Bi_2O_3 + CuO → $CuBi_2O_4$ begins at temperatures above ≈600 °C until $CuBi_2O_4$ melts incongruently to CuO + liquid at 820 ± 20 °C. These temperatures are too high for most commonly used glass-based transparent conductive substrates on which PEC photoelectrodes are typically deposited. The glass transition temperature, T_g, of typical soda-lime glass used for transparent conductive oxides (TCO) ranges between ≈540 and 570 °C.[42–44] The most commonly used TCO film is fluorine-doped SnO_2 (FTO), which its conductivity starts to decrease above ≈600 °C.[45,46] However, reports show that FTO remains stable at 800–1000 °C for short heating times (≈10^1–10^3 s).[43,47,48] Second, $CuBi_2O_4$ is a line compound (there is no $Cu_xBi_{2-x}O_4$ solid solution). Therefore, the formation of single-phase pure $CuBi_2O_4$ is not trivial, and the segregation of either CuO or Bi_2O_3 would occur when Bi:Cu stoichiometry ≠ 2.[32] As expected, the most common impurities are CuO,[34,49–52] and Bi_2O_3.[53–56] However, a non-stoichiometric $Cu_{0.84}Bi_{2.08}O_4$ was reported to form at low temperatures (≈200 °C) and to slowly decompose into Bi_2O_3 and $CuBi_2O_4$ at ≈400 °C.[55,57] The striking structural similarity between $CuBi_2O_4$ and $Cu_{0.84}Bi_{2.08}O_4$ is summarized in Table S1 and Figure S2 (Supporting Information). Note that CuO, Bi_2O_3, and $Cu_{0.84}Bi_{2.08}O_4$ are photoelectrochemically active materials. As mentioned (vide supra), uncontrollably formed, photoelectrochemically active impurities that are randomly intermixed with the desired photoabsorber material are potentially harmful to the photoelectrode integrity. The presence of impurities can influence the bandgap energy, charge carrier dynamics in the bulk (photogeneration, separation, and transport),[50] as well the surface (recombination vs catalysis),[58] and the photoelectrochemical stability of the photoelectrode.[32,59,60]

Recently, Feng et al. overviewed comprehensively different photoelectrochemical parameters of $CuBi_2O_4$ photocathodes synthesized by different chemical and physical techniques.[61] Parameters that fluctuate the most are the photoelectrochemical stability, bandgap energy (1.4–1.9 eV), and the incident photon-to-current efficiency (0.9–30% at 350 nm). All impurity

phases (CuO, Bi_2O_3, and $Cu_{0.84}Bi_{2.08}O_4$) were reported to form during chemical synthesis techniques that rely on a solvent, molecular precursor, and stabilizers, which are known to affect the formation mechanism, the films' morphology, and therefore, its electronic properties. However, in physical synthesis techniques of $CuBi_2O_4$, only Bi_2O_3 was reported as an impurity phase.[54] The structural, electronic, and photocatalytic properties of these impurity materials (primarily CuO and Bi_2O_3) are well studied. However, as photoelectrochemically active impurities randomly intermixed with the $CuBi_2O_4$ photoabsorber, little is known about their influence, primarily the effect of Bi_2O_3 that has six polymorphs with a range of electronic and ionic conductivity properties.[62,63] Three polymorphs (i.e., α-, β-, and δ-Bi_2O_3) have been reported to exhibit photocatalytic activity and to exist (as a single-phase or mixture, depending on growth conditions) in Bi_2O_3 thin films deposited by chemical and physical synthesis techniques.[64–72]

In this work, we present a new approach for synthesizing single-phase, high-quality complex metal oxide thin film photoelectrodes on FTO substrates and discuss the challenges involved in using $CuBi_2O_4$ as a case study material. We report a highly controllable synthesis route of phase-pure $CuBi_2O_4$ photoelectrodes by conducting a high-throughput combinatorial study of the relationship between the crystal structure, the synthesis conditions, and photoelectrochemical properties over a range of thicknesses. It was found that pure $CuBi_2O_4$ is formed after postdeposition annealing by rapid thermal processing (RTP) at 650 °C. In contrast, similar films heated up to 12 h by conventional furnace heating (FH) at 400 and 500 °C did not form a single phase. Pure $CuBi_2O_4$ photoelectrodes exhibit higher fill-factors, longer carrier lifetimes, higher photoconversion efficiencies, and increased stability than nonpure photoelectrodes. Additionally, pure $CuBi_2O_4$ showed an increase in photocurrent density with increased thicknesses until the photocurrents leveled off at ≈150 nm, displaying a photoresponse versus thickness behavior typical to a single-photoabsorber device. In the nonpure photoelectrodes, the formation of impurities was affected by the film thicknesses. However, despite increased charge separation efficiency in nonpure films and initial higher photoactivities, the photoactive impurities that are uncontrollably formed and randomly intermixed with the desired photoabsorber material can be harmful to the overall PEC performance.

2. Results and Discussion

To study the effect of different growth conditions on films of varying thicknesses, $CuBi_2O_4$ films with thickness gradients ("thickness libraries") were deposited on 50×50 mm^2 FTO substrates by pulsed laser deposition (PLD). A phase pure $CuBi_2O_4$ pellet was used as a target. Further details are provided in the Experimental Section and in Figures S3 and S4 (Supporting Information). The FTO substrates were not rotated during deposition and positioned away from the ablation plume center, which resulted in the desired thickness gradients.[73] The process is schematically described in **Figure 1**a, and an image of a library is shown in Figure 1b. High-throughput thickness measurements with energy dispersive X-ray spectrometry (EDS) in a scanning electron microscopy (SEM) confirmed a continuous gradient of ≈25–250 nm across the libraries, seen in Figure 1c. Dividing the libraries along their centerline (X = 22.5 mm) allows for postdeposition annealing ("annealing") by different treatments (i.e., RTP vs FH) of two symmetrical and identical sections, Figure 1d.

Figure 2a–c presents X-ray diffraction (XRD) contour maps of a $CuBi_2O_4$ library that was deposited at a substrate temperature of 500 °C, in which the two symmetrical sections of the library were annealed at different conditions. The presented 26.8°–35° 2Θ range contains the most dominant diffraction peaks of monoclinic α-Bi_2O_3, β-Bi_2O_3, $Cu_{0.84}Bi_{2.08}O_4$, and $CuBi_2O_4$ (color designated and marked as α, β, X, and C, respectively). The overlap between several closely spaced peaks between ≈28° and 33.3° requires careful deconvolution to assess the presence of the different phases. We note that the decomposition of $CuBi_2O_4$ and formation of CuO starts at temperatures of about 720 °C.[74,75] Therefore, the temperatures during the annealing of $CuBi_2O_4$ were kept significantly below 720 °C in our experiments (650 °C or less). Consequently, diffraction peaks of CuO were not observed for any of the films within the entire temperature range used for deposition and postdeposition annealing (400–650 °C), as seen in Figures S5 and S6 (Supporting Information). Figure 2a displays the map of a library section that was annealed by FH for 2 h at 500 °C in air. The peaks show crystalline $CuBi_2O_4$ at ≈28°, 29.7°, 30.7°, 32.5°, 33.3°, and 34.1° which correspond to the (211), (220), (002), (102), (310) and (112) lattice planes, respectively. Additionally, both the α-Bi_2O_3 and β-Bi_2O_3 phases are visible. The α-Bi_2O_3 phase is identified by the peaks at ≈26.9°, 27.3°, 28°, 32.4°, and 33.3° which correspond to the (111), (120), (012), (−211), and (200) lattice planes, respectively. The β-Bi_2O_3 phase is identified by the peaks at ≈28°, 30.3°, 31.8°, 32.7° corresponding to the (201), (211), (002), and (220) planes, respectively.

Figure 2b displays the contour map of a library section that was annealed by RTP for 1 min at 650 °C in one bar of oxygen. The peaks that correspond to both $CuBi_2O_4$ and α-Bi_2O_3 increase in intensity, whereas the intensity of the peaks corresponding to β-Bi_2O_3 decreases. Remarkably, after annealing the same library section for a total of 4 min by RTP, the two Bi_2O_3 phases have completely disappeared, as seen in Figures 2c and Figure S7 (Supporting Information). We note that a small peak centered at ≈28.8° appears after annealing at 650 °C, which has been previously assigned to FTO.[76] Despite this minor change, the transmittance and sheet resistance of bare FTO substrates were not affected by the RTP treatment, seen in Figure S8 (Supporting Information). To determine whether the formation of Bi_2O_3 is kinetically or thermodynamically controlled, an additional library was heated by FH for 12 h at 500 °C to evaluate if additional annealing time will form pure $CuBi_2O_4$. Note that 500 °C is the maximum temperature that the glass-based FTO substrates can withstand for extensive periods (several hours). Analysis of the library's composition shows that both Bi_2O_3 phases are still visible, seen in Figures S9a,c (Supporting Information). However, annealing the same library again by RTP for 4 min at 650 °C eliminates any evidence of the Bi_2O_3 phases, seen in Figure S9b,d (Supporting Information). Therefore, we conclude that Bi_2O_3 segregation is thermodynamically controlled, and heating at 650 °C leads to the formation of pure $CuBi_2O_4$ photoelectrodes.

Figure 2a also reveals that the α-Bi_2O_3 phase is primarily formed in the thicker films, whereas the β-Bi_2O_3 peaks are more prominent in the thinner films. To further understand

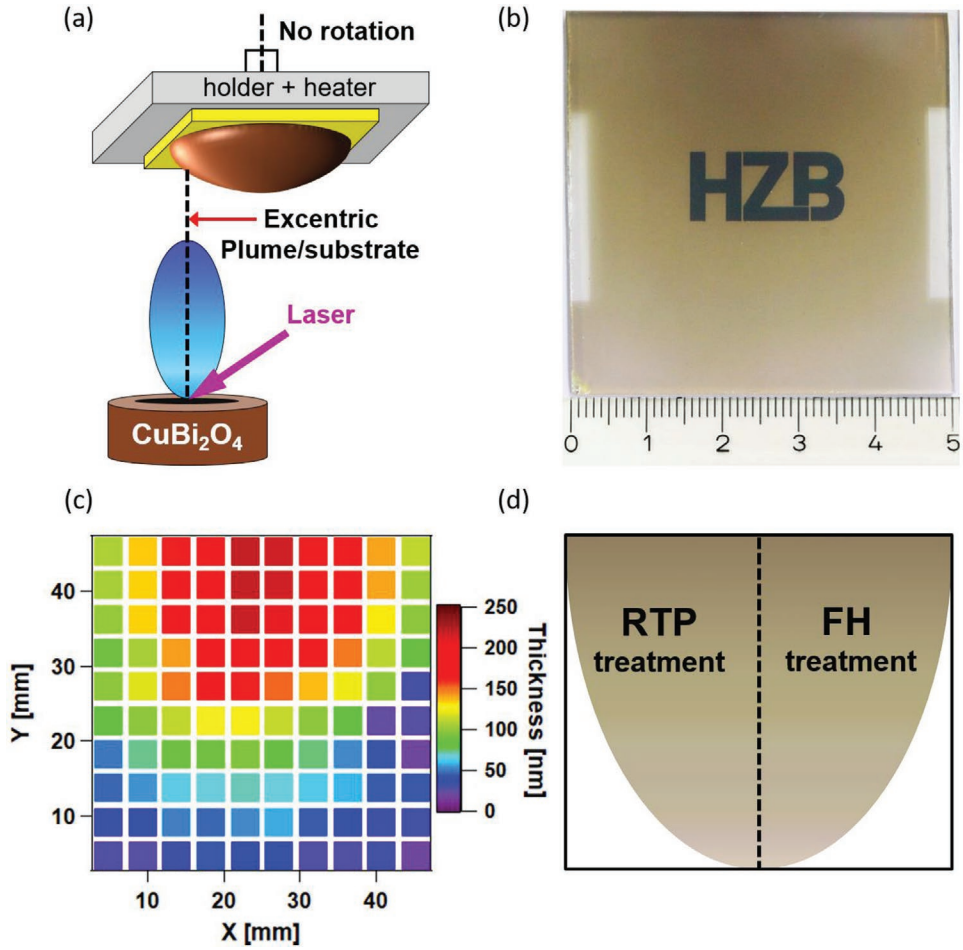

Figure 1. Illustration of the fabrication method of $CuBi_2O_4$ films with a thickness gradient ("thickness libraries") followed by different annealing treatments. a) Thin films of $CuBi_2O_4$ were deposited on large-area (50×50 mm^2) substrate by PLD, with thickness gradients created by positioning the substrate away from the ablation plume center. b) An image of a $CuBi_2O_4$ thickness library on an FTO substrate. c) A thickness map is showing a gradient of ≈25–250 nm. d) A schematic of a library divided at its center into two symmetrical and identical sections that would undergo different annealing treatments (i.e., RTP vs FH) for comparison.

how the temperature and film thickness affects these polymorphs of Bi_2O_3, a separate Bi_2O_3 library was made. The library was deposited at a substrate temperature of 500 °C and again divided into two symmetric sections. The two sections were annealed by FH and RTP, respectively. Figure 2d,e shows that α-Bi_2O_3 is the dominant phase in both annealing conditions. However, in the library annealed by FH at 500 °C, the intensity of the β-Bi_2O_3 peak centered at ≈28° (marked with *) is higher than for the library treated at 650 °C with RTP. The XRD analysis of both Bi_2O_3 libraries agrees with reports of the stable α- and metastable β-Bi_2O_3 polymorphs. The α-Bi_2O_3 phase is stable from room temperature up to ≈730 °C.[62] In contrast, the formation of β-Bi_2O_3 is reported to occur primarily at thicknesses below ≈150 nm, depending on the deposition and annealing conditions of Bi_2O_3 thin films grown by PLD and sputtering, between 250 and 500 °C.[66,67,69]

Figure 2f summarizes the X-ray diffraction results of the thickness libraries. The figure displays the diffractograms of the library regions that correspond to a film thickness of ≈120 nm, extracted from the contour maps in Figure 2a–c and from the libraries that were deposited at a substrate temperature of 400 °C and heated by FH 2 h at 400 °C in air. It is evident that crystalline, single-phase $CuBi_2O_4$ forms at 650 °C by RTP. Lower temperatures (400 °C) lead to poor crystallinity, and the formation of four impurities phases occurs: α, β-Bi_2O_3, $Cu_{0.84}Bi_{2.08}O_4$, and Bi_4O_7 are all present in Figure S10 (Supporting Information) (especially in the thinner films). To minimize phase impurities, we focus our efforts on films that were deposited at the maximum substrate temperature for glass-based FTO substrates (500 °C) from this point onward. To confirm our findings from the thickness libraries, $CuBi_2O_4$ and Bi_2O_3 films with homogenous thicknesses of 100 and 250 nm ($CuBi_2O_4$) and 150 nm (Bi_2O_3) were also deposited at 500°C on smaller (25×25 mm^2) FTO substrates and studied after similar annealing conditions as the thickness libraries. Figures S11 and S12 (Supporting Information) confirm identical findings. The only difference is that the thicker $CuBi_2O_4$films required slightly longer RTP times to achieve a pure $CuBi_2O_4$ phase.

Figure 3a–c shows color maps of the optical transmission, reflection, and absorbance for a thickness library after RTP at 650 °C. The maps are presented for $\lambda = 420$ nm as $CuBi_2O_4$, as well as all possible impurity phases, absorb at this wavelength (vide infra). Similar maps of a thickness library after FH at 500 °C and how the absorbance is calculated are seen

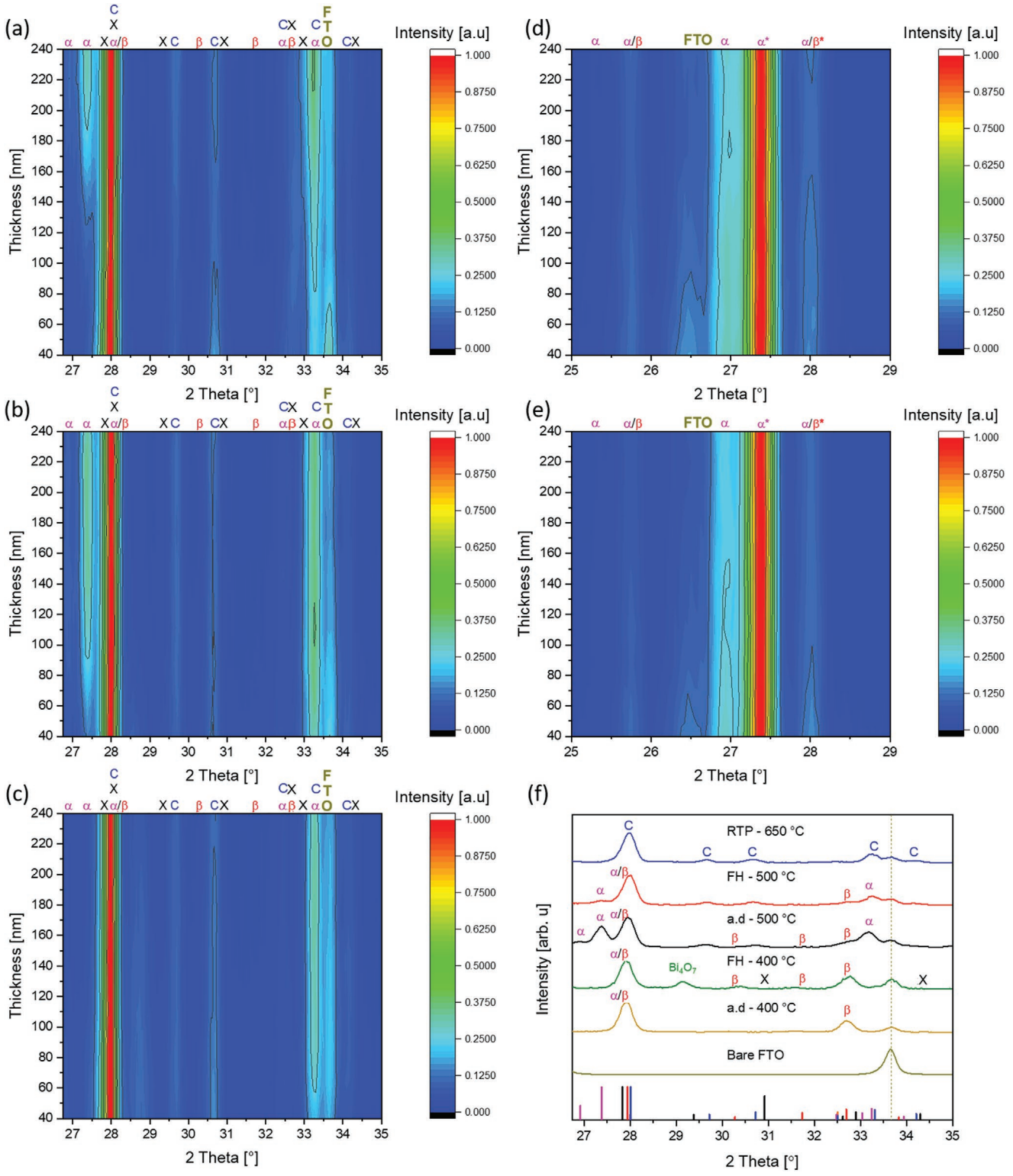

Figure 2. Left panel: X-ray diffraction contour maps showing the 26.8°–35° range of a $CuBi_2O_4$ thickness library that was deposited at a substrate temperature of 500 °C and annealed at different conditions. a) After FH for 2 h at 500 °C in air, b) after RTP for 1 min at 650 °C in one bar of oxygen, c) after RTP for 4 min at 650 °C in one bar of oxygen. Right panel: The contour maps showing the 26.8°–29° range of a Bi_2O_3 thickness library that was deposited at a substrate temperature of 500 °C and annealed at different conditions, d) after FH for 2 h at 500 °C in air, e) after RTP for 4 min at 650 °C in one bar of oxygen. f) X-ray diffractograms of areas of ≈120 nm thickness from five libraries, compared with a bare FTO substrate as a reference (a.d.—as deposited). The different phases are color designated and marked as α (α-Bi_2O_3, PDF card 00-041-1449, magenta), β (β-Bi_2O_3, PDF card 04-007-1443, red), X ($Cu_{0.84}Bi_{2.08}O_4$, PDF card 00-054-0009, black), C ($CuBi_2O_4$, PDF card 00-042-0334, blue), and Bi_4O_7 (PDF card 00-047-1058).

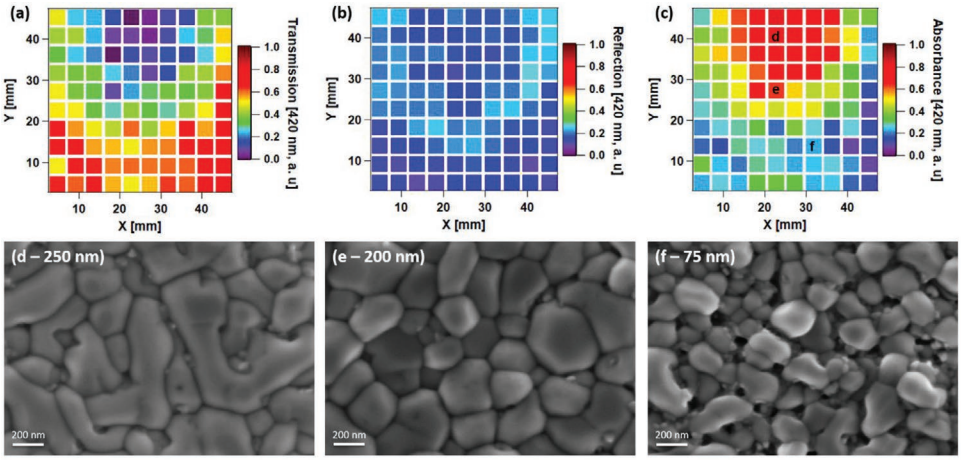

Figure 3. a–c) Color maps of the optical transmission, reflection, and absorbance for a thickness library after RTP at 650 °C. d–f) SEM images were taken at positions (d)–(f), respectively, as marked in (c). The thickness values shown were determined with energy dispersive X-ray spectrometry.

in Figure S13 (Supporting Information). General thickness dependence of the absorbance is seen across both the RTP and FH libraries. Note that a slight increase in absorbance is seen in the thinnest areas of both libraries ($Y \leq 10$ mm). This phenomenon results from optical interactions with the substrate and is wavelength and thickness dependent.[77] Figure 3d–f shows SEM images of three positions of different thicknesses in the library (d, e, and f), marked in Figure 3c. At all three thicknesses, the images show well-defined, faceted $CuBi_2O_4$ grains. At a thickness of 250 nm, the film is comprised of a mixture of elongated (long axis is 590 ± 90 nm) and pseudospherical grains (310 ± 30 nm). At a thickness of 200 nm, the average grain size is 320 ± 70 nm, with a pseudospherical morphology. At a thickness of 75 nm, the average grain size is 140 ± 50 nm, with a pseudo-spherical morphology, and the film appears to be less compact than in the thicker areas.

The effect of different annealing treatments on the films' morphology and absorption was studied in small-area films with homogenous thicknesses. **Figure 4**a–c shows top-view SEM images of 250 nm $CuBi_2O_4$ films: as-deposited, after FH for 2 h at 500 °C, and after RTP for 4 min 650 °C. The as-deposited film appears less compact, with poorly defined grains. In contrast, the annealed films appear more compact. The grains in the RTP-treated film are better defined and have

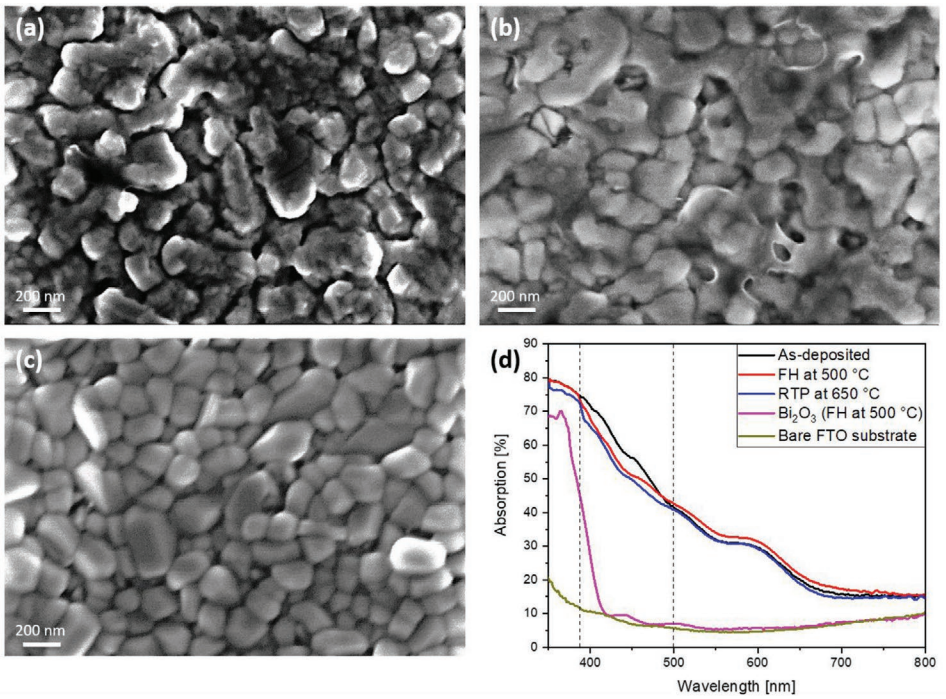

Figure 4. a) Electron microscopy of as-deposited $CuBi_2O_4$ at 500 °C, b) after FH for 2 h at 500 °C, c) after RTP for 4 min at 650 °C. d) Absorption of the three films compared with a 150 nm Bi_2O_3/FTO film and a bare FTO substrate as references. The area between the vertical dashed lines indicates the increased absorption range of the as-deposited film (≈385–500 nm).

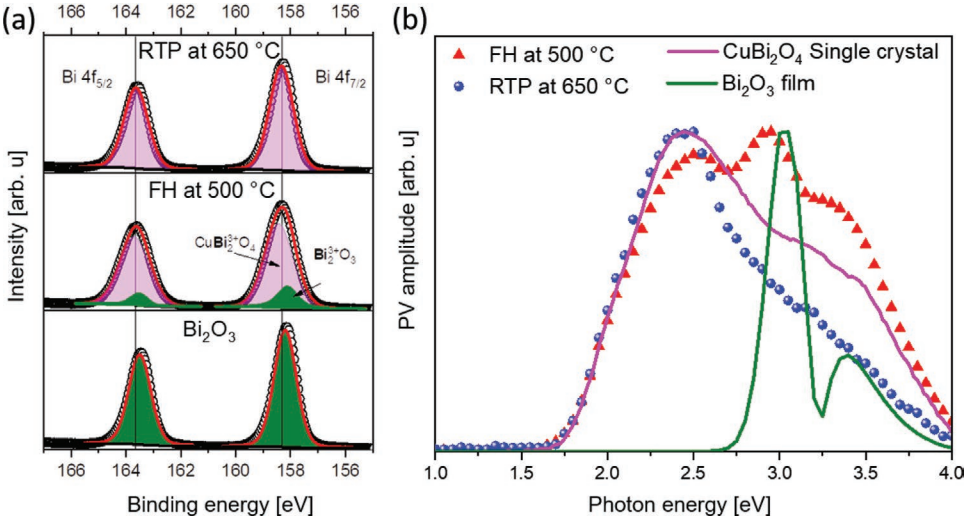

Figure 5. XPS spectra of a) Bi 4f core levels, from top to bottom: after RTP for 4 min at 650 °C in 1 bar of oxygen, after FH for 2 h at 500 °C in air, and α/β-Bi_2O_3 post-annealed by FH as a reference. The vertical lines are aligned with the peaks' centers in the RTP annealed sample. b) Spectra of modulated SPV of similar samples, with α/β-Bi_2O_3 film and a $CuBi_2O_4$ single crystal as references.

a narrower size distribution than the grains in the FH treated film. The latter seem larger and partially merged. Figure 4d shows the optical absorption spectra of the films. For comparison, the absorption of a 150 nm Bi_2O_3 film deposited on FTO, annealed by FH at 500 °C, is shown. The as-deposited $CuBi_2O_4$ film shows an increased absorption from 385 to 500 nm (the area between the two dashed lines), which correlates with the absorption of the Bi_2O_3 film. At longer wavelengths, the absorption of the as-deposited film was similar to the RTP-treated film except for a small tail above ≈635 nm (absorption edge of $CuBi_2O_4$), likely due to its poor crystallinity that can form tail states.[78] The absorption profiles of both annealed photoelectrodes were generally similar. However, the absorption of the FH-treated film is higher by ≈2–3% throughout the entire spectrum, which we attribute to its denser morphology and a possible minor contribution from Bi_2O_3 impurity.

The oxidation states of Bi and Cu at the surfaces of the photoelectrodes were studied by X-ray photoelectron spectroscopy (XPS). **Figure 5**a shows the Bi 4f core levels spectra of the FH and RTP annealed films with homogenous thicknesses of 250 nm, and an α/β-Bi_2O_3 film deposited on FTO and annealed by FH at 500 °C. In the RTP-treated film, a single Bi contribution is found, which corresponds to that found in $CuBi_2O_4$.[79] In contrast, the FH film showed two Bi^{3+} contributions, one that is found in $CuBi_2O_4$ and another one at slightly lower binding energies that have been reported for α/β-Bi_2O_3 films.[69,80] The Bi_2O_3 contribution disappears after RTP annealing. We also analyzed the XPS signals of Cu 2p, showing that the presence of Cu^{2+} is preserved in both samples, as seen in Figure S14a (Supporting Information). As reported before, a minor presence of Cu^{1+} was also seen in both samples. The XPS detailed fitting parameters are summarized in Figure S14b (Supporting Information).

To assess the optoelectronic quality and the bandgap energies of the films, intensity-modulated surface photovoltage (SPV) measurements were conducted on FH, and RTP treated films with homogenous thicknesses of 250 nm. An α/β-Bi_2O_3 film annealed by FH at 500 °C and a $CuBi_2O_4$ single crystal were used as references. The advantage of using intensity-modulated over steady-state SPV measurements is the ability to use lock-in detection, which results in a much higher sensitivity. Intensity-modulated measurements are susceptible to charge separation processes even in extremely thin photoactive layers or single nanocrystals, even though the absolute signal amplitudes are lower than for conventional steady-state Kelvin probe measurements. This allows probing the presence of electronic defects and the effect of minute compositional changes such as the additional presence of Bi_2O_3 in the nonpure photocathodes. Figure 5b displays the normalized SPV signals as a function of the photon energy. Plots showing the non-normalized signals and a detailed account of how to extract the bandgap energy appear in Figure S15 (Supporting Information). We find that the bandgaps of all films are similar to that of the single crystal, 1.90 ± 0.05 eV, consistent with previous reports.[32,81] The extracted bandgap of the α/β-Bi_2O_3 film is 2.85 ± 0.05 eV, which is in agreement with reported values of both α- and α/β films.[69,82] In the FH-treated film, an additional peak is seen at higher photon energies of ≈2.75–3.0 eV. This peak can be assigned to a small amount of Bi_2O_3, based on its overlap with the α/β-Bi_2O_3 film and the XPS data. In contrast, the RTP-treated film does not show a peak at those photon energies and had a remarkable similarity to the spectrum of the $CuBi_2O_4$ single crystal. Based on these results, from this point forward, we will refer to the RTP-treated films as "pure $CuBi_2O_4$" films and the FH-treated films as "nonpure" films.

Figure 6 presents photoelectrochemical studies conducted on 250 nm thick photoelectrodes, both from the same 25×25 mm^2 sample, that were annealed by FH and RTP. Figure 6a displays chopped linear sweep voltammetry (LSV) scans of both photoelectrodes, measured under AM1.5 illumination with H_2O_2 as an electron scavenger. Figure S16 (Supporting Information) displays the LSVs of both photoelectrodes without H_2O_2. We note that the photocurrent densities are modest in comparison to the benchmark values reported so far for $CuBi_2O_4$. However,

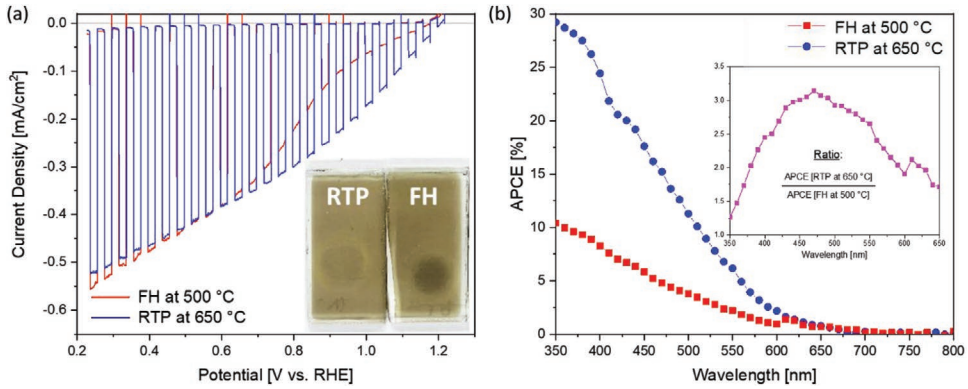

Figure 6. a) Chopped LSV scans of $CuBi_2O_4$ photoelectrodes deposited at 500 °C, after heating treatment of FH for 2 h at 500 °C, and after RTP for 4 min at 650 °C. The image shows both photoelectrodes after the LSVs. b) APCE measurements of both photoelectrodes performed at a bias of 0.6 V versus RHE using back-side illumination. The inset shows the APCE ratio between the two photoelectrodes. The presented scans were measured with H_2O_2 as an electron scavenger.

they agree with recently reported photocurrent densities of $CuBi_2O_4$ with similar thicknesses deposited by PLD.[81] We attribute the modest photocurrent densities mainly to their low specific surface area and absence of strategies to improve the photocurrent, such as doping (i.e., with Ag),[33] using selective contacts, and creating an internal gradient of copper vacancies, that were reported for these films.[34,51,54] The photocurrent densities of both photoelectrodes were similar, –0.38 mA cm^{-2} at 0.6 V versus RHE (back illumination), with onset potentials at ≈+1.2 V versus RHE.

Despite showing similar photocurrent densities, the fill-factor (FF) of the pure $CuBi_2O_4$ photoelectrode was higher, displaying higher current densities at lower applied potentials. The physical phenomena associated with the FF characteristics for a PEC device have been extensively studied.[4] They are closely related to surface recombination of electrons/holes and bulk recombination in the photoabsorber. Lower FF can qualitatively be used to predict lower performances over prolonged measurements (vide infra), despite similar photocurrent densities during rudimentary LSVs that can result from different (photo)electrochemical reactions. Furthermore, the pure $CuBi_2O_4$ photoelectrode did not show any visible signs of deterioration. It retained its appearance after the measurement, unlike the nonpure photoelectrode, which was shown to have darkened in the area that was exposed to the electrolyte. Stability measurements performed to both photocathodes for 4 h (without an electron scavenger) showed that the pure $CuBi_2O_4$ photoelectrode maintained higher photocurrents throughout the entire measurement period, seen in Figure S17 (Supporting Information). This demonstrates an enhanced photostability of the pure $CuBi_2O_4$ thin film photoelectrode, which is in agreement with our previous work on this material.[32] The flat-band potentials (φ_{fb}) of both photoelectrodes were estimated using Mott–Schottky measurements. Figure S18 (Supporting Information) shows Mott–Schottky plots of pure and nonpure photoelectrodes, measured at three different frequencies with similar slopes at each plot. The φ_{fb} of the pure $CuBi_2O_4$ photoelectrode is 1.25 V versus RHE, which is very close to the onset potential, and in agreement with previous reports.[33] However, the apparent φ_{fb} of the nonpure photoelectrode is 1.44 V versus RHE, which is ≈250 mV more positive than the photocurrent onset potential of the photoelectrode. This is opposite from what one would expect based on the chopped LSV scans in Figure S16 (Supporting Information), which show a slightly less positive photocurrent onset potential (and lower FF) for the nonpure samples. A less positive onset potential can be due to recombination in the space charge region or electron trapping at surface defects, both of which might indeed expect to occur in nonpure samples.[5] The reason for the discrepancy with the apparent φ_{fb} from the Mott–Schottky plots is, however, not clear. We point out that reliable quantitative interpretation of Mott–Schottky measurements is often hampered by the presence of surface states (which can shift the φ_{fb}) or incomplete ionization of acceptors (which leads to frequency dispersion). Since both effects may occur in our nonpure samples, we emphasize that the extrapolated values in the Mott-Schottky plot should be considered as apparent φ_{fb} at best.

Figure 6b displays the absorbed photon-to-current efficiency (APCE) of both photoelectrodes, measured at an applied bias of 0.6 V versus RHE. Applied bias photo-to-current efficiency is a straightforward diagnostic measurement to understand the material's performance and which photon energies contribute to the solar photocurrent (note that the chemical products are not directly measured).[83,84] The APCE onsets of both photoelectrodes were at 640 ± 10 nm (1.93 ± 0.03 eV), which corresponds with the measured bandgap energy and previous reports.[32,33] The overall shapes of the spectra are also similar to those previously reported for $CuBi_2O_4$. The main observation from Figure 6b is that the pure $CuBi_2O_4$ shows a 1.2–3 times higher APCE than the nonpure photoelectrode throughout the entire absorption spectrum. We tentatively attribute the lower photoconversion efficiency in the nonpure material to higher recombination due to the presence of α/β-Bi_2O_3 impurities in the nonpure photoelectrode. Figure S19a,b (Supporting Information) display the measured chopped currents and the calculated photocurrents used to determine the IPCE and APCE, displaying the higher (photo)currents of the pure $CuBi_2O_4$, despite showing similar photocurrent densities as the nonpure photoelectrode in the chopped LSV scans. The predicted AM1.5 photocurrent densities ($J_{AM1.5}$) were calculated from the IPCE data (see the Experimental Section), assuming the photocurrent depends linearly on the light intensity.[85] The predicted $J_{AM1.5}$

value of the pure $CuBi_2O_4$ was ≈–0.41 mA cm^{-2} (back illumination), compared to the measured photocurrent obtained by LSV of –0.38 mA cm^{-2} (back illumination). The predicted $J_{AM1.5}$ value for the nonpure $CuBi_2O_4$ films was ≈–0.30 mA cm^{-2} (back illumination), compared to the measured value obtained by LSV of –0.38 mA cm^{-2} (back illumination). The predicted $J_{AM1.5}$ value in the pure sample supported its corresponding photocurrent density. On the other hand, the predicted $J_{AM1.5}$ value in the nonpure sample was lower than its corresponding photocurrent density by ≈20%. This further supports our premise (vide supra) that similar photocurrent density during rudimentary LSVs can result from different (photo)electrochemical reactions.

Another observation is seen in the incident photon-to-current efficiency (IPCE) and additional APCE plots in Figure S19c,d (Supporting Information). Whereas the back-illuminated IPCE/APCE show large differences between the pure and nonpure samples, the front-illuminated IPCE/APCE are almost identical. This seems either to suggest that the RTP treatment is particularly effective at improving minority carriers transport or that the impurities in the nonpure samples impede minority carrier transport. Based on these results and the fact that the nonpure samples contain impurities intermixed with the $CuBi_2O_4$ photoabsorber, further studies beyond the scope of this work are required to differentiate between recombination processes at the bulk versus at the surface.

The carrier transport properties of FH and RTP treated films deposited on quartz glasses were investigated using time-resolved microwave conductivity (TRMC) measurements.[86] TRMC can be used to determine charge carrier mobilities and lifetimes on time-scales from ns to ms. It is a contactless technique suitable for comparing the transport properties of photoexcited charge carriers of different photoabsorber materials. TRMC is primarily a bulk-sensitive technique but can also be used to study charge carrier transfer across interfaces. It is often used to study processes that limit transport, such as carrier trapping and recombination at grain boundaries.[13,87–90] In our TRMC setup, films are excited with a laser pulse at $\lambda = 420$ nm, and the resulting light-induced change in the reflected microwave power is monitored. The obtained TRMC signal represents the product of the absorbance-normalized quantum yield (ϕ) and the sum of the mobilities of free charge carriers in the film (see the Experimental Section for details). We note that ϕ should not be confused with the internal photoconversion efficiency (APCE) determined by photocurrent measurements, where carriers are collected at the external contacts. Assuming that the internal quantum yield (ϕ) is close to unity and that no recombination occurs within the response time of the setup (≈8–10 ns), the peak value of the TRMC signal reflects the total mobility, which is the sum of the charge carrier mobilities of both electrons and holes. The TRMC signal decay is often used to determine the carrier lifetime (τ), although in some materials, it may be due to a decrease in the mobility (instead of the number) of the charge carriers (due to, e.g., trapping).

Figure 7 shows the TRMC signals ($\phi\Sigma\mu$ vs time) for 250 nm films with homogenous thicknesses. The X-ray diffractograms of the films and their analysis are presented in Figure S20 (Supporting Information). The highest TRMC signals are obtained for the FH film, reaching maximum amplitudes of 4.8×10^{-4} cm^2 V^{-1} s^{-1}. However, the signal shows a short initial

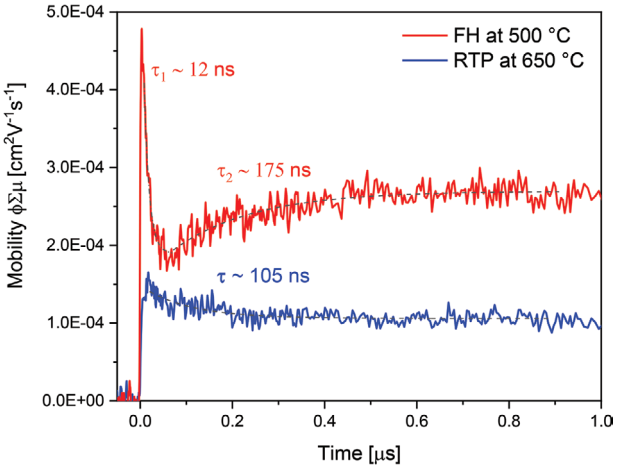

Figure 7. TRMC signals for 250 nm films deposited on quartz substrates: after heating treatment of FH for 2 h at 500 °C, and after RTP for 4 min at 650 °C.

lifetime (τ_1) of 12 ns. Furthermore, a subsequent rise in signal amplitude ($\tau_2 \approx 175$ ns) following the initial decay was visible. In contrast, the RTP-treated film exhibit a smaller amplitude of 1.65×10^{-4} cm^2 V^{-1} s^{-1}, with a single lifetime of $\tau \approx 105$ ns. The time constant and signal amplitude of the RTP-treated sample are consistent with previously reported values for $CuBi_2O_4$.[34,38]

The higher signal amplitudes and shorter lifetimes in the FH treated film indicate that the charge transfer processes in its bulk are different from in the RTP treated film. Two possible mechanisms would explain higher signal amplitudes: i) increased optical absorption by the phase impurities (mainly α/β-Bi_2O_3), or ii) improved charge separation efficiency of photoexcited carriers in the phase impurities. However, the mobilities quantification already includes the absorption data of the films, which makes the latter the only possible mechanism. Therefore, additional TRMC measurements were performed to 75, 150, and 250 nm Bi_2O_3 films to examine their signal amplitudes and lifetimes, seen in Figure S21 (Supporting Information). Their signals show maximum amplitudes of 3.8, 5, and 2.73×10^{-4} cm^2 V^{-1} s^{-1} (75, 150, and 250 nm, respectively), which were higher than the RTP-treated film. Note that the 75 nm Bi_2O_3 sample shows a similar amplitude to the FH-treated $CuBi_2O_4$ film (vide supra). Additionally, all signals have decay times shorter than 20 ns and therefore comparable to the initial decay in the FH-treated $CuBi_2O_4$ film. Thus, the carrier mobilities in single-phase $CuBi_2O_4$ are lower than in Bi_2O_3 films (which are mixtures of the α- and β polymorphs), but their lifetimes are longer. Based on these results, we conclude that the higher amplitudes and initial fast decays in the FH sample originate from a contribution of Bi_2O_3 phase impurities. Next, we discuss the increase in the signal after ≈60 ns in the FH sample. This process occurs after the photoexcitation by the laser pulse (i.e., in the dark), and there is no further excitation and no photogeneration of mobile carriers. This increase is uncommon but was reported before (vide infra). We believe that after ≈60 ns, one type of charge carrier is injected from the $CuBi_2O_4$ into the Bi_2O_3 impurity phase, as Bi_2O_3 is behaving as a selective contact. Within the Bi_2O_3, as shown in Figure S21 (Supporting Information), the charge carriers have

higher mobility than in the $CuBi_2O_4$ phase. As only one carrier is mobile in the Bi_2O_3 phase (carries of opposite charge either already recombined or were injected to another phase as well), fewer recombination events are expected, which is the reason for the signal increase. Our interpretation is reinforced by a similar rise in signal previously characterized as injection processes from one crystal phase to another.[87,88] In contrast, the RTP treated film does not show this signal increase, which indicates that this impurity phase is absent, which is consistent with our previous results (i.e., XRD, XPS, and SPV).

High-throughput photoelectrochemical measurements of the photocurrent densities of pure and nonpure libraries were conducted using an automated optical scanning droplet cell (OSDC). Details of this setup are described elsewhere.[91] With the OSDC, the photocurrent can be measured for a large number of locations on the sample with millimeter resolution, which allows us to correlate the photoactivity of the material to its structural properties.[30,92] Figures S22–S24 (Supporting Information) show the major components of the OSDC and how the effective surface area of the miniature PEC cell was calibrated. **Figure 8** shows photocurrent densities, measured at 0.6 V versus RHE, plotted versus thicknesses for three pure $CuBi_2O_4$ libraries (Figure 8a), and three nonpure $CuBi_2O_4$ libraries (Figure 8b). All three libraries in Figure 8a show an increase in photocurrent density with increased thicknesses until the photocurrent levels off at ≈150 nm, above which it seems to decrease slightly. The initial increase is due to an increase in optical absorption as the films grow thicker. When the thickness exceeds the minority carrier diffusion length, the photocurrent no longer increases. The data in Figure 8a suggest that the minority carrier diffusion length of these phase-pure $CuBi_2O_4$ films is ≈150 nm.

The nonpure libraries did not show a significant influence of the film thickness on the photocurrent (Figure 8b). Surprisingly, the highest photocurrents are already obtained for the thinnest films (25 nm), and the photocurrent decreases by about 10% when the thickness increases to 220 nm. When comparing Figure 8a,b, the most striking difference is the lower photocurrent for the phase-pure films for thicknesses below ≈100 nm. Since the thinnest films also show the largest concentration of phase impurities (see discussion of Figure 2), the presence of phase impurities may explain the higher photocurrent. Two possible mechanisms would explain this: i) increased optical absorption by the phase impurities (mainly α/β-Bi_2O_3), or ii) improved charge separation efficiency by injection of photoexcited carriers from $CuBi_2O_4$ into the impurity phase. An accurate determination of the absorption coefficient across the libraries requires highly smooth surfaces of both substrate and films, which is not the case in this study (see discussion of Figures 3 and 4). Therefore, only an "effective absorption coefficient" can be currently considered to examine the optical absorption in both libraries. Figure S25 (Supporting Information) shows thickness, transmission, reflection, and "effective absorption coefficient" (α_{eff}) maps at 420 nm for a pure and nonpure library. Extracted values of α_{eff} from four different positions across the libraries show a slight increase in thinner films. However, the α_{eff} values are slightly higher in the pure $CuBi_2O_4$ library, which informs us that the higher photocurrents of the nonpure library do not result from increased absorption of impurity phases. For that reason, the likely mechanism is an improved charge separation efficiency by injection of photoexcited carriers from $CuBi_2O_4$ into the impurity phase, which is already supported by our TRMC analysis (vide infra). To further support our hypothesis, photoelectrochemical measurements were performed on Bi_2O_3 photoelectrodes with thicknesses of 75 and 200 nm, seen in Figure S26 (Supporting Information). The 75 nm Bi_2O_3 photoelectrode showed a higher photocurrent density than the 200 nm photoelectrode (–0.18 compared with –0.11 mA cm^{-2}). At 75 nm, the combined photocurrent densities of a single-phase $CuBi_2O_4$ (Figure 8a, 0.15 ± 0.05 mA cm^{-2}) and the 75 nm Bi_2O_3 photoelectrode are ≈0.28–0.33 mA cm^{-2}. This value is slightly higher than the average values in the nonpure libraries at 75 nm (Figure 8b, 0.2 ± 0.05 mA cm^{-2}). However, the lower values in the nonpure library can be due to increased recombination in the multiple-phase film. Based on these results and the higher carrier mobilities of the nonpure film (see discussion of Figure 7), we conclude that the higher photocurrent densities in the nonpure thin films originate from an increased charge separation efficiency in the phase impurities (mainly α/β-Bi_2O_3). Despite that, we wish to highlight that the randomly intermixed α/β-Bi_2O_3 impurities are expected to degrade the overall PEC performance, as shown in the APCE and stability measurements.

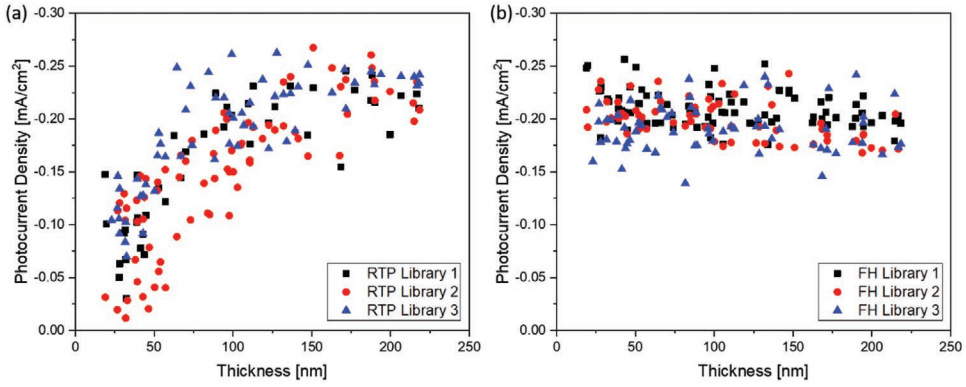

Figure 8. Photocurrent densities (at 0.6 V vs RHE) plotted as a function thickness in a) pure $CuBi_2O_4$ libraries and b) nonpure $CuBi_2O_4$ + α/β-Bi_2O_3 libraries.

3. Conclusions

We presented an approach to overcome phase-purity challenges in complex metal-oxides, showing the importance of attaining a single-phase multinary compound by exploring large growth parameter-spaces, achieved by employing a combinatorial approach to study $CuBi_2O_4$, a prime candidate photoabsorber for solar water splitting due to its attractive electronic properties. To enable discovering the exact conditions under which pure photoelectrodes are formed, a high-throughput combinatorial study of the relationship between the crystal structure, different synthesis conditions, and properties over a range of thicknesses was performed. Single-phase $CuBi_2O_4$ photoelectrodes were obtained by PLD and postannealing by RTP at 650 °C with a thickness range of 25–250 nm, showing that radiative annealing is essential in controlling phase purity without damaging the FTO coated glass substrate. In contrast, similar films heated by a conventional furnace at 400 and 500 °C resulted in the segregation of photoactive impurities (Bi_4O_7, $Cu_{0.84}Bi_{2.08}O_4$, α-, and β-Bi_2O_3), which was affected by the films' thicknesses. Intensity-modulated SPV measurements of pure and nonpure films determined band-gap energies of 1.90 ± 0.05 eV, similar to the value of a single crystal. However, the presence of impurities at the films' surfaces was identified by both SPV and XPS. Phase-pure $CuBi_2O_4$ photoelectrodes exhibited higher fill factors, photoconversion efficiencies, enhanced stabilities, and longer carrier lifetimes than the nonpure photoelectrodes. In addition, pure $CuBi_2O_4$ showed an increase in photocurrent density with increased thicknesses until the photocurrents leveled off at about 150 nm. Surprisingly, nonpure photoelectrodes showed the highest photocurrents already for the thinnest films (25 nm), owing to improved charge separation efficiency in the impurity phases and due to their higher photoactivities shown by TRMC and photoelectrochemical analysis. However, despite increased charge separation efficiency in nonpure films and initial higher photoactivities, it is shown that photoactive impurities that are uncontrollably formed and randomly intermixed with the desired photoabsorber material can be harmful to the overall PEC performance. Our work demonstrates the prosperous perspective of pure $CuBi_2O_4$ as a photoabsorber material. From a broader perspective, the high-throughput combinatorial approach combined with radiative annealing techniques paves the way toward new synthesis routes of single-phase, highly efficient multinary photoelectrodes and nanostructured materials with enhanced carrier transport and novel functionalities.

4. Experimental Section

Film Deposition: $CuBi_2O_4$ films were deposited using a PLD system (PREVAC, Poland) by ablating from a $CuBi_2O_4$ target with a KrF-Excimer laser (248 nm, LPXPro 210, COHERENT). The target was prepared by traditional ceramic methods, based on a previous report.[93] Equimolar amounts of CuO and Bi_2O_3 powders (99.9%, Alfa Aesar) were mixed in a ball mill for 1 h, and pressed at a force of 100 kN under vacuum into a pellet with a diameter of 30 mm, and sintered in air at 700 °C for 24 h. The process was repeated three times (the temperatures in the 2nd and 3rd repetitions were 750 and 800 °C, respectively), until the target showed no impurities, Figures S3 and S4 (Supporting Information). Bi_2O_3 was deposited from a commercial target (99.99%, MaTeck). All films were deposited at a substrate temperature of either 400 or 500 °C. The laser fluence was 1 J cm^{-2}, and the repetition rate was 10 Hz. An oxygen background pressure (PO_2) of 1×10^{-2} mbar was used and the target-to-substrate distance was 60 mm. The substrates were FTO-coated glass (TEC 7, Pilkington) or quartz (Spectrosil 2000, Baumbauch & Co LTD), cleaned in a 1 vol % Triton solution (Triton X-100, Sigma-Aldrich), deionized water, and ethanol (≥99.99%, Sigma-Aldrich) for 10 min in each solution.

Crystal Growth: $CuBi_2O_4$ crystals were grown by the floating zone technique in a four mirror optical image furnace (Crystal Systems Corp., Japan), in ambient air at a rate of 5 mm h^{-1}. The high-density feed rod ($D \approx 6$ mm, $L \approx 7$ cm) was prepared from a stoichiometric mixture of high purity powders of Bi_2O_3 (99.99%) and CuO (99.995%) by a solid-state reaction.

Furnace Heating and Rapid Thermal Processing: Conventional furnace heating of the films was performed at either 400 or 500 °C in air at a heating rate of 10 °C min^{-1}. Rapid thermal processing (RTP) was conducted using a Rapid Thermal Processor (model: AS-One 100, ANNEALSYS). All RTP treatments were performed under atmospheric pressure of pure oxygen, with a heating rate of 10 °C s^{-1}. In a typical RTP procedure, a sample was placed on a SiC wafer, used as a susceptor, with an optical pyrometer monitoring the temperature of the SiC. Additionally, surface temperatures of the samples were monitored by a thermocouple attached to the surface with an indium contact. To eliminate any concern of losing Bi_2O_3 during heating due to its high volatility,[94] inductively coupled plasma mass spectrometry (ICP-MS) measurements of dissolved films confirmed an identical Bi:Cu ratio in all samples.

Characterization: XRD measurements of films with homogenous thicknesses were performed using a Bruker D8 diffractometer with Cu Kα radiation. The $CuBi_2O_4$ target and scanning measurements were conducted using a Panalytical X'Pert Pro MPD using Cu Kα radiation. Measurements were carried out in a grazing incidence geometry (angle of incidence was 2°) with a step size of 0.04° and a step duration of 6 s. The data were normalized after removing the background, without additional data averaging or noise reduction. The $CuBi_2O_4$ target was analyzed by Raman microscopy (Dilor micro LabRam, Horiba) with a laser excitation wavelength of 635 nm and a power of 0.6 mW at the objective (spot size: ≈1 µm in diameter). XPS were performed with a SPECS PHOIBOS 100 analyzer at base pressure of $\approx 10^{-10}$ mbar. Monochromatic Al Kα radiation (hn = 1486.74 eV, SPECS FOCUS 500 monochromator) was applied with the pass energy of 30 and 10 eV. The step sizes were chosen to be 0.5 eV for the survey and 0.05 eV for the fine spectra. For fitting the peaks, XPSPEAK software with Voigt profiles and a Shirley background subtraction was applied. The adventitious carbon (C 1s) peak at binding energy of 284.5 eV was used for the calibration of binding energies.

UV–vis measurements were performed using a PerkinElmer Lambda 950 spectrophotometer with an integrating sphere. Samples were placed inside the integrating sphere with an offset of ≈7.5° from the incident light, and the transflectance TR (transmittance T + reflectance R) was measured. The absorptance and absorption coefficient were calculated as follows

$$\text{Absorptance} = 1 - \text{transflectance} \quad (1)$$

$$\text{Absorption coefficient}, \alpha = \frac{-\ln(\text{transflectance})}{d_{\text{eff}}} \quad (2)$$

where d_{eff} is the effective thickness.

The high-throughput optical measurement were conducted in an optical scanner, similar to the one described elsewhere.[77] The scanner is capable of measuring total transmission and total reflection with millimeter special resolution.

SEM imaging was carried out at a Zeiss UltraPlus or at a LEO GEMINI 1530 scanning electron microscope operated at 7 or 5 kV acceleration voltage. The grains size was measured by using the ImageJ software. The high-throughput thickness determination of libraries was performed

using EDS measurements in the SEM, using the Oxford Instruments AZtec LayerProbe software to process the data.[95,96] A series of 100 EDS spectra (10 × 10 grid) was acquired from the large area sample. The LayerProbe software refines a starting model of the layered structure against the EDS spectra, to calculate the thickness and composition of each of the layers. The starting model comprises the layer sequence in the sample and the chemical composition of the layers. Control measurements were performed with SEM imaging of individual cross-sections of samples, as well with a DEKTAK profilometer resulted in similar thickness values with an accuracy of ±5 nm.

Modulated surface photovoltage (SPV) spectra were measured in the configuration of a parallel plate capacitor (quartz cylinder partially coated with the SnO_2:F electrode, mica sheet as an insulator), in an ambient atmosphere.[97] The SPV signal is defined as the change in the surface potential as a result of the illumination. Front illumination (light impinging the surface) was provided by a halogen lamp, coupled to a quartz prism monochromator (SPM2), and modulated at a frequency of 8 Hz by using an optical chopper. In-phase and 90° phase-shifted SPV signals were detected with a high-impedance buffer and a dual-phase lock-in amplifier (EG&G 5210). The amplitude of the modulated SPV signal is defined as the square root of the sum of the squared in-phase and 90° phase-shifted SPV signals.[98]

Photoelectrochemical measurements were performed in the three-electrode configuration under the control of a potentiostat (EG&G Princeton Applied Research 273A). The studied films were connected as the working electrode in a custom-designed PEC cell with a calibrated Ag/AgCl reference electrode (XR300, Radiometer Analytical, $E_{Ag/AgCl}$ = 0.199 V versus normal hydrogen electrode, NHE), and a platinum wire as the counter electrode. All the measured potentials were converted to the reversible hydrogen electrode (RHE) scale using the Nernst equation. The illuminated area of the sample was 0.28 cm^2, which is identical to the area exposed to the electrolyte. The optical scanning droplet cell, which was used to perform high-throughput photoelectrochemical measurements, was manufactured by Sensolytics GmbH, Bochum, Germany. Linear sweep voltammetry scans were performed in 100 points (10 × 10 grid) across a typical large-area sample. The measured photocurrent densities at 0.6 V versus RHE were plotted versus thicknesses. All measurements were performed in an aqueous 0.3 M K_2SO_4 and 0.2 M phosphate buffer (pH 7). Measurements with H_2O_2 as an electron scavenger were performed with 30% hydrogen peroxide (Merck Schuchardt oHG) that was mixed with the electrolyte in a 4:1 (electrolyte:H_2O_2) volume ratio. A WACOM super solar simulator (Model WXS-50S-5H, class AAA) was used as the illumination source and calibrated to closely resemble the AM1.5 global spectrum at 100 mW cm^{-2}. Stability measurements were performed under chopped light at 0.6 V versus RHE, without H_2O_2.

For incident photon-to-current efficiency (IPCE) measurements, a LOT (LSH302) lamp and Acton Research monochromator (SP2150) were used. The incident-photon-to-current conversion efficiency (IPCE) values were calculated as follows

$$\text{IPCE}\ (\%) = \frac{J_P\left(\text{mA cm}^{-2}\right) \times 1240\left(\text{V nm}\right)}{P\left(\text{mW cm}^{-2}\right) \times \lambda\left(\text{nm}\right)} \times 100 \tag{3}$$

where J_P is the averaged photocurrent density, P is the power density of the incident light, and λ is the wavelength. The power density was calibrated through the electrolyte contained between two quartz windows for front side illumination and through FTO glass for backside illumination. This means that the reported IPCE values are for the $CuBi_2O_4$ film itself and not for the entire $CuBi_2O_4$ photocathode/PEC cell assembly. Absorbed photon-to-current efficiency (APCE) values were calculated by dividing the IPCE through the absorptance (see Equation (2)) of the measured photoelectrode (corrected for the absorptance of the FTO glass) as follows

$$\text{APCE}\ (\%) = \frac{\text{IPCE}(\%)}{\text{Absorptance}} \tag{4}$$

The predicted AM1.5 photocurrent density $J_{AM1.5}$ (mA cm^{-2}) of the photoelectrodes was estimated by multiplying the IPCE values with the solar photon flux $\Phi_{AM1.5}$ (mA cm^{-2} nm^{-1}) and integrating it over the measured wavelengths, according to Equation (5)

$$J_{AM1.5} = \int_{350\text{nm}}^{850\text{nm}} [\text{IPCE}(\lambda) \times \Phi_{AM1.5}(\lambda)]\text{d}\lambda \tag{5}$$

TRMC measurements of $CuBi_2O_4$ deposited on quartz substrates were carried out using X-band (8400–8700 MHz) microwaves generated by an voltage-controlled oscillator (Sivers IMA VO3262X) as a probe and a wavelength-tunable optical parametric oscillator (OPO) coupled to a diode-pumped Q-switched Nd:YAG laser (EKSPLA NT230-50-SH/ SF) as the excitation source. The wavelength was 420 nm, the pulse length was 3 ns (full-width at half-maximum). The laser fluence was 30 μJ cm^{-2}, and thus the resulting number of photons exciting the sample in a single pulse was $I_0 = 6.3 \times 10^{13}$ photons cm^{-2}. During the measurements, a change in the microwave power ($\Delta P/P$) reflected by the cavity upon sample excitation was monitored and correlated to the photoinduced change in the conductance of the sample, ΔG, given by

$$\frac{\Delta P}{P}(t) = -K\Delta G(t) \tag{6}$$

where K is the sensitivity factor of the cavity that is calculated from an analytical formula according to previously published report.[99] From the experimentally observed change in the photoconductance, the product of the charge carrier generation yield (φ) and the sum of electron and hole mobilities ($\Sigma\mu$) can be obtained from the equation[99]

$$\varphi\sum_i \mu_i = \frac{\Delta G}{\beta e I_0 F_a} \tag{7}$$

where I_0 is the incident intensity per pulse, β is a geometrical factor of the cavity, e the elementary charge, and F_a is the fraction of incident photons absorbed within the sample. A more detailed description of the TRMC measurements, setup, and analysis can be found elsewhere.[100,101] The photoconductivity signals of the samples were normalized with respect to the amount of absorbed photons, which were obtained from the product of the incident photon intensity and the absorptance (F_a) of the $CuBi_2O_4$ films deposited on quartz. For the mobility quantification, the charge carrier generation yield (φ) was assumed to be 1.

Supporting Information

Supporting Information is available from the Wiley Online Library or from the author.

Acknowledgements

The authors would like to acknowledge Fatwa F. Abdi for fruitful discussions, Rene Gunder for XRD user support, Thomas Unold, Pascal Becker, Dorian Drevon, Moritz Kölbach, and Karsten Harbauer for technical support. The authors also thank A. T. M. Nazmul Islam for providing the $CuBi_2O_4$ single crystals, and Eliran Evenstein, Marine Cornet, and David Kérinec for their experimental assistance.

Open access funding enabled and organized by Projekt DEAL.

Conflict of Interest

The authors declare no conflict of interest.

Data Availability Statement

Research data are not shared.

Keywords

complex metal oxides, $CuBi_2O_4$, pulsed laser deposition, radiative heating, rapid thermal processing, solar water splitting

Received: November 3, 2020
Revised: January 7, 2021
Published online:

[1] A. Fujishima, K. Honda, *Nature* **1972**, *238*, 37.
[2] J. R. Bolton, *Science* **1978**, *202*, 705.
[3] J. R. Bolton, S. J. Stricklert, J. Connolly, *Nature* **1985**, *316*, 495.
[4] M. G. Walter, E. L. Warren, J. R. McKone, S. W. Boettcher, Q. Mi, E. A. Santori, N. S. Lewis, *Chem. Rev.* **2010**, *110*, 6446.
[5] R. van de Krol, M. Grätzel, *Photoelectrochemical Hydrogen Production* (Eds:R. v. d. Krol, M. Grätzel), Springer, New York **2012**.
[6] J. H. Kim, D. Hansora, P. Sharma, J. W. Jang, J. S. Lee, *Chem. Soc. Rev.* **2019**, *48*, 1908.
[7] F. F. Abdi, S. P. Berglund, R. van de Krol, in *Photoelectrochemical Solar Fuel Production: From Basic Principles to Advanced Devices*, (Eds: S. Giménez, J. Bisquert), Springer International Publishing, New York **2016**, pp. 355–391.
[8] F. F. Abdi, S. P. Berglund, *J. Phys. D: Appl. Phys.* **2017**, *50*, 193002.
[9] D. K. Lee, D. Lee, M. A. Lumley, K. S. Choi, *Chem. Soc. Rev.* **2019**, *48*, 2126.
[10] J. T. Devreese, A. S. Alexandrov, *Rep. Prog. Phys.* **2009**, *72*, 066501.
[11] A. J. E. Rettie, W. D. Chemelewski, D. Emin, C. B. Mullins, *J. Phys. Chem. Lett.* **2016**, *7*, 471.
[12] Y. Natanzon, A. Azulay, Y. Amouyal, *Isr. J. Chem.* **2020**, *60*, 768.
[13] J.-W. Jang, D. Friedrich, S. Müller, M. Lamers, H. Hempel, S. Lardhi, Z. Cao, M. Harb, L. Cavallo, R. Heller, R. Eichberger, R. van de Krol, F. F. Abdi, *Adv. Energy Mater.* **2017**, *7*, 1701536.
[14] C. Jiang, S. J. A. Moniz, A. Wang, T. Zhang, J. Tang, *Chem. Soc. Rev.* **2017**, *46*, 4645.
[15] Y. Pihosh, I. Turkevych, K. Mawatari, J. Uemura, Y. Kazoe, S. Kosar, K. Makita, T. Sugaya, T. Matsui, D. Fujita, M. Tosa, M. Kondo, T. Kitamori, *Sci. Rep.* **2015**, *5*, 11141.
[16] Y. Chen, X. Feng, Y. Liu, X. Guan, C. Burda, L. Guo, *ACS Energy Lett.* **2020**, *5*, 844.
[17] A. Bianconi, N. Poccia, *J. Supercond. Novel. Magn.* **2012**, *25*, 1403.
[18] J. Yuan, V. Stanev, C. Gao, I. Takeuchi, K. Jin, *Supercond. Sci. Technol.* **2019**, *32*, 123001.
[19] R. van de Krol, B. A. Parkinson, *MRS Energy Sustainability* **2017**, *4*, E13.
[20] J. E. Katz, T. R. Gingrich, E. A. Santori, N. S. Lewis, *Energy Environ. Sci.* **2009**, *2*, 103.
[21] M. Woodhouse, B. A. Parkinson, *Chem. Soc. Rev.* **2009**, *38*, 197.
[22] Q. Yan, J. Yu, S. K. Suram, L. Zhou, A. Shinde, P. F. Newhouse, W. Chen, G. Li, K. A. Persson, J. M. Gregoire, J. B. Neaton, *Proc. Natl. Acad. Sci. USA* **2017**, *114*, 3040.
[23] L. Zhou, A. Shinde, D. Guevarra, J. A. Haber, K. A. Persson, J. B. Neaton, J. M. Gregoire, *ACS Energy Lett.* **2020**, *5*, 1413.
[24] S. Kumari, R. Gutkowski, J. R. C. Junqueira, A. Kostka, K. Hengge, C. Scheu, W. Schuhmann, A. Ludwig, *ACS Comb. Sci.* **2018**, *20*, 544.
[25] G. Spinolo, U. Anselmi-Tamburini, P. Ghigna, G. Flor, *Physica C* **1993**, *217*, 347.
[26] E. Borvick, A. Y. Anderson, H. N. Barad, M. Priel, D. A. Keller, A. Ginsburg, K. J. Rietwyk, S. Meir, A. Zaban, *ACS Comb. Sci.* **2017**, *19*, 755.
[27] J. L. MacManus-Driscoll, M. P. Wells, C. Yun, J.-W. Lee, C.-B. Eom, D. G. Schlom, *APL Mater.* **2020**, *8*, 040904.
[28] G. Abadias, E. Chason, J. Keckes, M. Sebastiani, G. B. Thompson, E. Barthel, G. L. Doll, C. E. Murray, C. H. Stoessel, L. Martinu, *J. Vac. Sci. Technol., A* **2018**, *36*, 020801.
[29] H. Fan, Z. Li, M. Huang, X. Zhang, *Int. J. Solids Struct.* **2011**, *48*, 1754.
[30] L. Gouda, K. J. Rietwyk, J. Hu, A. Kama, A. Ginsburg, M. Priel, D. A. Keller, S. Tirosh, R. Gottesman, A. Zaban, *ACS Energy Lett.* **2017**, *2*, 2356.
[31] T. Arai, Y. Konishi, Y. Iwasaki, H. Sugihara, K. Sayama, *J. Comb. Chem.* **2007**, *9*, 574.
[32] R. Gottesman, A. Song, I. Levine, M. Krause, A. T. N. Islam, D. Abou-Ras, T. Dittrich, R. van de Krol, A. Chemseddine, *Adv. Funct. Mater.* **2020**, *28*, 1910832.
[33] D. Kang, J. C. Hill, Y. Park, K. S. Choi, *Chem. Mater.* **2016**, *28*, 4331.
[34] F. Wang, W. Septina, A. Chemseddine, F. F. Abdi, D. Friedrich, P. Bogdanoff, R. van de Krol, S. D. Tilley, S. P. Berglund, *J. Am. Chem. Soc.* **2017**, *139*, 15094.
[35] Y. Wang, H. Wang, A. R. Woldu, X. Zhang, T. He, *Catal. Today* **2019**, *335*, 388.
[36] V. Kumaravel, J. Bartlett, S. C. Pillai, *ACS Energy Lett.* **2020**, *5*, 486.
[37] L. Pan, J. H. Kim, M. T. Mayer, M. K. Son, A. Ummadisingu, J. S. Lee, A. Hagfeldt, J. Luo, M. Grätzel, *Nat. Catal.* **2018**, *1*, 412.
[38] S. P. Berglund, F. F. Abdi, P. Bogdanoff, A. Chemseddine, D. Friedrich, R. van de Krol, *Chem. Mater.* **2016**, *28*, 4231.
[39] C.-F. Tsang, J. K. Meen, D. Elthon, *J. Am. Ceram. Soc.* **1994**, *77*, 3119.
[40] B. Hallstedt, D. Risold, L. J. Gauckler, *J. Am. Ceram. Soc.* **1996**, *79*, 353.
[41] V. V. Belousov, A. A. Klimashin, *Russ. Chem. Rev.* **2013**, *82*, 273.
[42] S. HX, T. Rouxel, M. Buckley, C. Bernard, *J. Mater. Res.* **2006**, *21*, 632.
[43] J. K. Kim, S. U. Chai, Y. Cho, L. Cai, S. J. Kim, S. Park, J. H. Park, X. Zheng, *Small* **2017**, *13*, 1702260.
[44] J. Shen, D. J. Green, R. E. Tressler, D. L. Shelleman, *J. Non. Cryst. Solids* **2003**, *324*, 277.
[45] T. Kawashima, T. Ezure, K. Okada, H. Matsui, K. Goto, N. Tanabe, *J. Photochem. Photobiol., A* **2004**, *164*, 199.
[46] W. H. Baek, M. Choi, T. S. Yoon, H. H. Lee, Y. S. Kim, *Appl. Phys. Lett.* **2010**, 96, 133506.
[47] S. Park, J. H. Baek, L. Zhang, J. M. Lee, K. H. Stone, I. S. Cho, J. Guo, H. S. Jung, X. Zheng, A. C. S. Sustain, *Chem. Eng.* **2019**, *7*, 5867.
[48] S. Sánchez, M. Vallés-Pelarda, J. A. Alberola-Borràs, R. Vidal, J. J. Jerónimo-Rendón, M. Saliba, P. P. Boix, I. Mora-Seró, *Mater. Today* **2019**, *31*, 39.
[49] Y. Xu, J. Jian, F. Li, W. Liu, L. Jia, H. Wang, *J. Mater. Chem. A* **2019**, *7*, 21997.
[50] Z. Zhang, S. A. Lindley, R. Dhall, K. C. Bustillo, W. Han, E. Xie, J. K. Cooper, *ACS Appl. Energy Mater.* **2019**, *2*, 4111.
[51] A. Song, P. Plate, A. Chemseddine, F. Wang, F. Abdi, M. Wollgarten, R. van de Krol, S. Berglund, *J. Mater. Chem. A* **2019**, *7*, 9183.
[52] L. Zhu, P. Basnet, S. R. Larson, L. P. Jones, J. Y. Howe, R. A. Tripp, Y. Zhao, *ChemistrySelect* **2016**, *1*, 1518.
[53] N.-W. Kim, B.-U. Choi, H. Yu, S. Ryu, J. Oh, *Opt. Express* **2019**, *27*, A171.
[54] J. O., S. L. Jongmin Lee, H. Yoon, S. Kim, S. Seo, J. Song, B.-U.k Choi, S. Y.o. Choi, H. Park, S. Ryu, *Chem. Commun.* **2019**, *55*, 12447.
[55] N. Henry, O. Mentre, J. C. Boivin, F. Abraham, *Chem. Mater.* **2001**, *13*, 543.
[56] F. Wang, A. Chemseddine, F. Abdi, R. van de Krol, S. Berglund, *J. Mater. Chem. A* **2017**, *5*, 12838.
[57] H. Tang, Z. Dai, X. Xie, Z. Wen, R. Chen, *Chem. Eng. J.* **2019**, *356*, 472.
[58] C. Zachäus, F. F. Abdi, L. M. Peter, R. Van De Krol, *Chem. Sci.* **2017**, *8*, 3712.
[59] F. Nandjou, S. Haussener, *J. Phys. D: Appl. Phys.* **2017**, *50*, 124002.
[60] G. Sharma, Z. Zhao, P. Sarker, B. A. Nail, J. Wang, M. N. Huda, F. E. Osterloh, *J. Mater. Chem. A* **2016**, *4*, 2936.

[61] K. Feng, E. M. Akinoglu, F. Bozheyev, L. Guo, M. Jin, X. Wang, G. Zhou, M. J. Naughton, M. Giersig, *J. Phys. D: Appl. Phys.* **2020**, *53*, 495501.
[62] M. Drache, P. Roussel, J. P. Wignacourt, *Chem. Rev.* **2007**, *107*, 80.
[63] S. Sanna, V. Esposito, J. W. Andreasen, J. Hjelm, W. Zhang, T. Kasama, S. B. Simonsen, M. Christensen, S. Linderoth, N. Pryds, *Nat. Mater.* **2015**, *14*, 500.
[64] Y. Qiu, M. Yang, H. Fan, Y. Zuo, Y. Shao, Y. Xu, X. Yang, S. Yang, *CrystEngComm* **2011**, *13*, 1843.
[65] S. Gong, Q. Han, X. Wang, J. Zhu, *CrystEngComm* **2015**, *17*, 9185.
[66] L. Leontie, M. Caraman, A. Visinoiu, G. I. Rusu, *Thin Solid Films* **2005**, *473*, 230.
[67] B. L. Zhu, X. Z. Zhao, *Opt. Mater.* **2006**, *29*, 192.
[68] E. T. Salim, Y. Al-Douri, M. S. Al Wazny, M. A. Fakhri, *Sol. Energy* **2014**, *107*, 523.
[69] Y. C. Liang, K. J. Chiang, *CrystEngComm* **2020**, *22*, 4215.
[70] L. C. Tien, Y. H. Liou, *Surf. Coatings Technol.* **2015**, *265*, 1.
[71] B. Sirota, J. Reyes-Cuellar, P. Kohli, L. Wang, M. E. McCarroll, S. M. Aouadi, *Thin Solid Films* **2012**, *520*, 6118.
[72] J. C. Medina, M. Bizarro, C. L. Gomez, O. Depablos-Rivera, R. Mirabal-Rojas, B. M. Monroy, A. Fonseca-Garcia, J. Perez-Alvarez, S. E. Rodil, *Catal. Today* **2016**, *266*, 144.
[73] D. A. Keller, A. Ginsburg, H.-N. Barad, K. Shimanovich, Y. Bouhadana, E. Rosh-Hodesh, I. Takeuchi, H. Aviv, Y. R. Tischler, A. Y. Anderson, A. Zaban, *ACS Comb. Sci.* **2015**, *17*, 209.
[74] C. Changkang, H. Yongle, B. M. Wanklyn, J. W. Hodby, F. R. Wondre, *J. Mater. Sci.* **1993**, *28*, 5045.
[75] V. V. Belousov, *J. Am. Ceram. Soc.* **1996**, *79*, 1703.
[76] J. K. Yang, B. Liang, M. J. Zhao, Y. Gao, F. C. Zhang, H. L. Zhao, *Sci. Rep.* **2015**, *5*, 1.
[77] A. Y. Anderson, Y. Bouhadana, H. N. Barad, B. Kupfer, E. Rosh-Hodesh, H. Aviv, Y. R. Tischler, S. Rühle, A. Zaban, *ACS Comb. Sci.* **2014**, *16*, 53.
[78] S. K. O'Leary, S. R. Johnson, P. K. Lim, *J. Appl. Phys.* **1997**, *82*, 3334.
[79] F. E. Oropeza, B. T. Feleki, K. H. L. Zhang, E. J. M. Hensen, J. P. Hofmann, *ACS Appl. Energy Mater.* **2019**, *2*, 6866.
[80] Y. Shi, L. Luo, Y. Zhang, Y. Chen, S. Wang, L. Li, Y. Long, F. Jiang, *Ceram. Int.* **2017**, *43*, 7627.
[81] J. Lee, H. Yoon, K. S. Choi, S. Kim, S. Seo, J. Song, B. Choi, J. Ryu, S. Ryu, J. Oh, C. Jeon, S. Lee, *Small* **2020**, 16, 2002429.
[82] J. Eberl, H. Kisch, *Photochem. Photobiol. Sci.* **2008**, *7*, 1400.
[83] Z. Chen, T. F. Jaramillo, T. G. Deutsch, A. Kleiman-Shwarsctein, A. J. Forman, N. Gaillard, R. Garland, K. Takanabe, C. Heske, M. Sunkara, E. W. McFarland, K. Domen, E. L. Miller, J. a. Turner, H. N. Dinh, *J. Mater. Res.* **2010**, *25*, 3.
[84] K. Sivula, R. van de Krol, *Nat. Rev. Mater.* **2016**, *1*, 15010.
[85] J. Nelson, *The Physics of Solar Cells*, Imperial College Press, London **2003**.
[86] F. F. Abdi, T. J. Savenije, M. M. May, B. Dam, R. Van De Krol, *J. Phys. Chem. Lett.* **2013**, *4*, 2752.
[87] A. Ramírez, D. Friedrich, M. Kunst, S. Fiechter, *Chem. Phys. Lett.* **2013**, *568–569*, 157.
[88] M. Kunst, T. Moehl, F. Wünsch, H. Tributsch, *Superlattices Microstruct.* **2006**, *39*, 376.
[89] M. Kölbach, H. Hempel, K. Harbauer, M. Schleuning, A. Petsiuk, K. Höflich, V. Deinhart, D. Friedrich, R. Eichberger, F. F. Abdi, R. van de Krol, *ACS Appl. Energy Mater.* **2020**, *3*, 4320.
[90] M. Ziwritsch, S. Müller, H. Hempel, T. Unold, F. F. Abdi, R. Van De Krol, D. Friedrich, R. Eichberger, *ACS Energy Lett.* **2016**, *1*, 888.
[91] K. Sliozberg, D. Schäfer, T. Erichsen, R. Meyer, C. Khare, A. Ludwig, W. Schuhmann, *ChemSusChem* **2015**, *8*, 1270.
[92] R. Meyer, K. Sliozberg, C. Khare, W. Schuhmann, A. Ludwig, *ChemSusChem* **2015**, *8*, 1279.
[93] P. Ghigna, U. Anselmi-Tamburini, G. Spinolo, G. Flor, *J. Phys. Chem. Solids* **1993**, *54*, 107.
[94] M. A. Zurbuchen, J. Lettieri, S. J. Fulk, Y. Jia, A. H. Carim, D. G. Schlom, *Appl. Phys. Lett.* **2003**, *82*, 4711.
[95] C. Lang, S. Rühle, A. Y. Anderson, A. Zaban, P. Statham, S. Burgess, *Microsc. Microanal.* **2013**, *19*, 1872.
[96] C. Poulter, C. Lang, *Microsc. Microanal.* **2014**, *20*, 1836.
[97] T. Dittrich, A. Gonzáles, T. Rada, T. Rissom, E. Zillner, S. Sadewasser, M. Lux-Steiner, *Thin Solid Films* **2013**, *535*, 357.
[98] V. Duzhko, V. Y. Timoshenko, F. Koch, T. Dittrich, *Phys. Rev. B: Condens. Matter Mater. Phys.* **2001**, *64*, 752041.
[99] T. J. Savenije, A. J. Ferguson, N. Kopidakis, G. Rumbles, *J. Phys. Chem. C* **2013**, *117*, 24085.
[100] H. Stein, S. Müller, K. Schwarzburg, D. Friedrich, A. Ludwig, R. Eichberger, *ACS Appl. Mater. Interfaces* **2018**, *10*, 35869.
[101] S. States, M. S. Prevot, X. A. Jeanbourquin, W. S. Bouree, F. Abdi, R. Van De Krol, N. Guijarro, F. L. Formal, K. Sivula, *Chem. Mater.* **2017**, *29*, 4952.